

Microscopic Structures of Tri-*n*-butyl Phosphate/*n*-Octane Mixtures by X-ray and Neutron Scattering in a Wide *q* Range

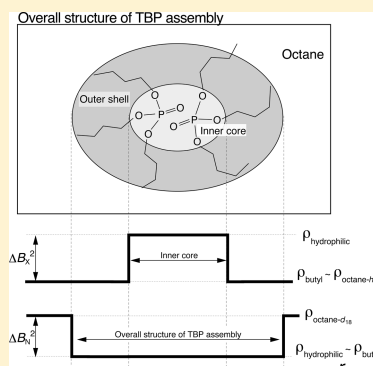
Ryuhei Motokawa,^{*,†} Shinichi Suzuki,[†] Hiroki Ogawa,[‡] Mark R. Antonio,[§] and Tsuyoshi Yaita[†]

[†]Actinide Coordination Chemistry Group, Quantum Beam Science Directorate (QuBS), Japan Atomic Energy Agency (JAEA), Ibaraki 319-1195, Japan

[‡]Japan Synchrotron Radiation Research Institute (JASRI)/SPring-8, 1-1-1 Koto, Sayo-cho, Sayo-gun, Hyogo 679-5148, Japan

[§]Chemical Sciences & Engineering Division, Argonne National Laboratory, Argonne, Illinois 60439, United States.

ABSTRACT: Tri-*n*-butyl phosphate (TBP) is an important extractant for separating hexavalent uranium and tetravalent plutonium from used nuclear fuel by solvent extraction. In such solvent extractions using TBP, the organic phase occasionally separates into two organic phases, namely, light and heavy organic phases. The latter one in particular is called the third phase. The purpose of this work is to elucidate the mechanism whereby the third phase forms in biphasic liquid–liquid solvent extraction of heavy metal ions. Toward this end, small- and wide-angle X-ray and neutron scattering (SWAXS and SWANS) experiments were conducted to examine the microscopic structures of TBP/octane mixtures. These investigations of solute associations in TBP-containing organic phases before extraction of heavy metal ions provide insights into system performance. After the extraction of heavy metal ions, for example, the microscopic structures formed in the organic phase are likely to be correlated with the initial microscopic structures, which are revealed here. SWAXS and SWANS, with accurate estimations of incoherent scattering intensities for all solution samples, revealed the following: (i) TBP self-associates in octane, and the average distance between two TBP molecules in the TBP assemblies is evaluated as 0.9–1.0 nm; (ii) the shape of the TBP assembly is ellipsoidal; and (iii) the attractive interaction among TBP assemblies in octane is miniscule, and thus, they tend to be dispersed homogeneously due to the excluded volume effect.



1. INTRODUCTION

Tri-*n*-butyl phosphate (TBP) is an important extractant for separating hexavalent uranium, U(VI), and tetravalent plutonium, Pu(IV), from used nuclear fuel by solvent extraction.¹ In such solvent extractions, the organic phase occasionally separates into two organic phases, namely, light and heavy organic phases. The heavy organic phase in particular is called the third phase.^{2,3} It contains high concentrations of U(VI), Pu(IV), and TBP. In essence, the third phase is formed by reverse micelles of TBP, where the reverse micelle core is capable of incorporating heavy metal ions. Third phase formation in the extraction process could lead to a criticality accident and hinder the safe and stable operation of used fuel reprocessing facilities. Accordingly, understanding the mechanism of third phase formation, in conjunction with the microscopic structure of TBP reverse micelles, is important. Moreover, third phase formation can be regarded as an important and intriguing phenomenon not only from the practical viewpoint described above but also from a fundamental one. The characteristic features of the reverse micelles formed in the extracted organic phase play a major role in third phase formation. Therefore, in a biphasic system for liquid–liquid extraction of heavy metal ions, third phase formation can be understood by considering the organic phase as a complex fluid, involving high-order structures, rather than as a simple molecular solution. Through small- and wide-angle

X-ray and neutron scattering (SWAXS and SWANS)^{4–7} observations of TBP/octane mixtures, this work contributes to contemporary knowledge of third phase formation mechanisms as well as to clarifying the microscopic structure of TBP reverse micelles in organic phases.

The combined method of SWAXS and SWANS^{6–8} used in this study is a powerful tool for investigating the microscopic structures of TBP/octane mixtures, as will be explained in detail in Section 3-1. SWAXS enables observation of the scattering contrast between the hydrophilic inner core of TBP assemblies and the other parts (i.e., the hydrophobic outer shell of the TBP assemblies and octane), whereas SWANS enables observation of the scattering contrast between TBP assemblies and octane. Accordingly, this combined method is capable of providing a detailed picture of both the hydrophilic inner core and the overall structure of the TBP assembly.

Osseo-Asare⁹ reviewed the experimental evidence, reported before 1991, of the existence of self-associated species in TBP/diluent systems.^{10–19} The self-association of TBP has been observed by various experimental techniques including partitioning studies,¹⁰ infrared spectroscopy,¹¹ nuclear magnetic resonance,¹² calorimetry,^{14–16} and vapor pressure osmome-

Received: November 9, 2011

Revised: December 31, 2011

Published: January 3, 2012



try.¹³ These experiments revealed that the self-association of TBP is attributable to dipole–dipole interactions involving the P=O groups of the phosphate ester mediated by hydrogen bonding with water, forming TBP dimers.^{1,10–12,18–20} Moreover, in that review⁹ on TBP–diluent/H₂O–acid–metal ion extraction systems, Osseo-Asare proposed that the TBP–acid–metal ion complex consists of a high-order assembly (reverse micelle or microemulsion) in organic diluents. The self-assembled architecture is composed of a hydrophilic core (P=O groups of TBP), which incorporates heavy metal ions, and a hydrophobic shell (butyl groups of TBP), which is swollen by diluent. At that time in 1991, however, little was known of the structural information (size, shape, and aggregation number) or characteristic features of these high-order assemblies in the organic phase, and thus, the origin of the third phase formation was not fully explained.

Since 1998, based on the pioneering work of Osseo-Asare,⁹ initial progress in understanding third phase formation was achieved through direct observations of organic phases containing extracted heavy metal ions by small-angle X-ray and neutron scattering (SAXS and SANS) techniques. Using the Baxter sticky hard sphere model^{21–24} to quantitatively analyze the scattering profiles, Erlinger et al. examined the microscopic structures of reverse micelles of malonamides in organic phases. As a result, they proposed that third phase formation originates from van der Waals interactions between malonamide reverse micelles in the organic phase.²⁵ Along similar lines, Chiarizia, Jensen, and their co-workers have applied the Baxter sticky hard sphere model to small-angle scattering profiles^{26–39} obtained for organic phases containing TBP and heavy metal ions, to study the mechanism of third phase formation. Despite the success of the micellar interaction model, further study is needed to identify the characteristics and microscopic structures of the constituent micelles. Baxter's model can accurately reproduce the high scattering intensities in the low- q region ($q < 1.0 \text{ nm}^{-1}$), where $q = (4\pi/\lambda)\sin(\theta)$ is the magnitude of the scattering vector \mathbf{q} with a scattering angle 2θ and an incident X-ray or neutron beam of wavelength λ . In the high- q region ($q > 1.0 \text{ nm}^{-1}$), however, the SAXS and SANS profiles tend to deviate from those calculated with this model.^{36,37,40–42} In addition, the scattering maximum that originates from interparticle interferences among the reverse micelles in Baxter's model has not been clearly identified in experimental data before now.

In this work, we describe the microscopic structure of TBP assemblies in a dry diluent through analyses of the SAXS and SANS profiles obtained from the TBP extraction systems and, thereby, provide original insights into the mechanism of third phase formation. To do this, we collected SWAXS and SWANS data for a number of TBP/octane mixtures as a function of the volume fraction of TBP, ϕ_{TBP} . Investigating the microscopic structures in the TBP/octane model system provides an important glimpse into the initial state of the organic phase before extraction of heavy metal ions. After solvent extraction of heavy metal ions, the microscopic structure of TBP reverse micelles should depend upon and show correlation with the initial state of the TBP/octane mixture. Nevertheless, as far as we know, the microscopic structures of TBP/octane mixtures have never been directly observed by scattering techniques.

Here, after presenting the experimental methods, we report and discuss the findings pertaining to the SWAXS and SWANS studies. We would like to emphasize that the structural information and characteristic features are expected to be

useful in analyzing SAXS and SANS profiles obtained for TBP reverse micelles that incorporate heavy metal ions in their core. The results of this study contribute to the evolving understanding of the micellar model of third phase formation.

2. EXPERIMENTAL SECTION

2-1. Materials and Sample Preparation. TBP (Tokyo Kasei; purity, >99%), *n*-octane (Wako; purity, >98%), and *n*-octane-*d*₁₈ (Aldrich; purity, >98%) were dried overnight over 4A molecular sieves (Wako) before use. TBP and *n*-octane were mixed in vial tubes at various ϕ_{TBP} values ranging from 0 to 1; then, each solution was analyzed by SWAXS, SWANS, and viscosity measurements.

2-2. Small- and Wide-Angle X-ray Scattering (SWAXS). SWAXS measurements were performed at BL-40B2 of SPring-8 (Japan Synchrotron Radiation Institute, Harima, Japan).⁴³ With a double-crystal Si(111) monochromator, the incident X-ray beam was monochromatized so that the wavelength, λ , was 0.1 nm (12.39 keV) and the wavelength distribution, $\Delta\lambda/\lambda$, was 10^{-4} . At the sample position, the X-ray beam was focused to a spot size of about $200 \mu\text{m} \times 100 \mu\text{m}$ (horizontal \times vertical, full width at half-maximum). The scattered X-rays from the sample were detected by two two-dimensional detectors: an imaging plate (IP; R-Axis IIV, Rigaku) with 3000×3000 pixels and a CMOS flat panel sensor (FPS; C9728DK, Hamamatsu Photonics) with 1032×1032 pixels ($52.8 \text{ mm} \times 52.8 \text{ mm}$) that, respectively, covered the low- q range ($0.2 \text{ nm}^{-1} < q < 2.5 \text{ nm}^{-1}$) and the high- q range ($0.15 \text{ nm}^{-1} < q < 40 \text{ nm}^{-1}$). The sample-to-detector distance was set at 1.5 m for IP and 66.3 mm for FPS. The scattering data recorded with IP and FPS were corrected for counting efficiency, instrumental background, and air scattering on a pixel-to-pixel basis; the X-ray scattering intensity distribution was circularly averaged. The scattering intensity profiles obtained with IP were converted to absolute units of reciprocal centimeters (cm^{-1}) by using a glassy carbon standard.⁴⁴ The scattering intensity profiles observed by the FPS detector were converted to the scale of the IP detector to clearly show their q dependence, where the absolute scattered intensity distribution is designated as $I(q)$ hereafter. The sample solutions were sealed in glass capillary cells of 0.01 mm wall thickness and 2.0 mm sample thickness. All X-ray scattering data were acquired at 25 °C.

2-3. Small- and Wide-Angle Neutron Scattering (SWANS). SWANS measurements were performed with the EQ-SANS spectrometer, installed at BL-6, Spallation Neutron Source (SNS), at Oak Ridge National Laboratory (ORNL), United States.⁴⁵ EQ-SANS covers a q range of $0.1 \text{ nm}^{-1} < q < 14 \text{ nm}^{-1}$ at a sample-to-detector distance of 1.3 m in a 30 Hz frame-skipping mode with the minimum incident neutron wavelength λ set to 0.2 nm, giving a maximum wavelength of 1.4 nm, by using a time-of-flight technique. With a pinhole slit collimator, the incident neutron beam of 25 mm diameter was cut and shaped into a circular beam of 9 mm diameter. The scattered neutrons were detected with a two-dimensional position-sensitive ³He detector of $1.0 \text{ m} \times 1.0 \text{ m}$, composed of tube detectors providing 256×192 pixels. The scattering data were corrected for counting efficiency, instrumental background, and air scattering, on a pixel-to-pixel basis. The scattered neutron intensity distribution was circularly averaged by taking into account the λ dependence of the transmittance of neutrons in samples. We converted the scattering intensities to absolute units of reciprocal centimeters (cm^{-1}) by using a porous SiO₂ powder standard. Incoherent scattering from

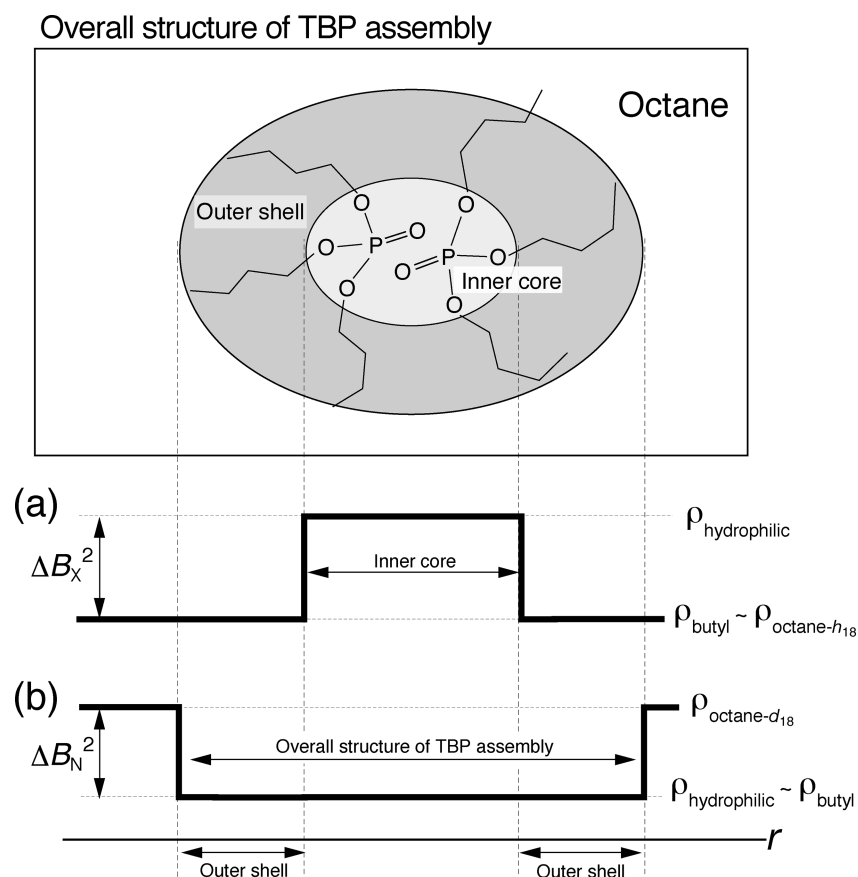


Figure 1. Schematic of TBP assembly, consisting of a hydrophilic core of phosphate esters (light gray) and a hydrophobic shell of butyl groups (dark gray), in octane, and schematic of the spatial distribution of scattering contrast (a) ΔB_X^2 for X-rays across a TBP assembly in octane- h_{18} and (b) ΔB_N^2 for neutrons across a TBP assembly in octane- d_{18} .

hydrogen, estimated as a constant value from the incoherent scattering intensity (I_{inc}) of a reference sample (octane- h_{18}) in a quartz cell with 2 mm sample thickness, was subtracted from the net absolute intensity [$I_{\text{coh+inc}}(q)$]. It shows that the q dependence of the coherent scattering intensity [$I_{\text{coh}}(q)$] dramatically changes, before and after subtracting I_{inc} from $I_{\text{coh+inc}}(q)$, and the details will be explained in Section 3-2.

SWANS experiments were carried out with octane- d_{18} solutions to ensure sufficient neutron scattering contrast between TBP and octane- d_{18} and to minimize the incoherent scattering background from hydrogen. The sample solutions were sealed in quartz cells of 2.0 mm sample thickness. All neutron scattering data were acquired at 25 °C, the same as for the X-ray scattering measurements.

2-4. Viscosity Measurement. The solutions for viscosity measurements were prepared with the same volume ratios of TBP/ n -octane as those for SWAXS measurements. Viscosity was measured on an Ubbelohde-type capillary viscometer as a function of ϕ_{TBP} in the range from 0 to 1.0 at 25 ± 0.05 °C. The time required for the meniscus to travel between two points was recorded, which is proportional to the viscosity. The specific viscosity, η_{sp} , is given by $\eta_{\text{sp}} = (\eta - \eta_0)/\eta_0$, where η and η_0 are the viscosities of the TBP/ n -octane- h_{18} mixtures and octane- h_{18} , respectively.

3. RESULTS AND DISCUSSION

3-1. X-ray and Neutron Scattering Length Densities of TBP/Octane Mixtures. To investigate the microscopic structure of the TBP/octane mixtures with different ϕ_{TBP}

values, both SWAXS and SWANS measurements were employed in this study. In many ways, neutron scattering complements X-ray scattering in the study of material structures, mainly because the neutron cross section varies randomly among elements, whereas the X-ray atomic scattering factor increases with atomic number. The large difference in the scattering cross section between hydrogen and deuterium in particular is crucial in the use of neutron scattering techniques.^{6,7}

The X-rays scattered by the phosphorus atom of TBP in octane- h_{18} overwhelm the scatterings from the other elements. Conversely, with neutrons, the use of octane- d_{18} provides sufficient scattering contrast between TBP and octane- d_{18} . Figure 1 shows a schematic of the fundamental unit of the TBP assemblies in octane as well as diagrams for the spatial distribution of the scattering contrast for (a) X-rays, ΔB_X^2 , and (b) neutrons, ΔB_N^2 . The model assumes that (i) with X-rays the scattering length densities between the hydrophobic butyl groups in TBP (ρ_{butyl}) and octane- h_{18} ($\rho_{\text{octane-}h_{18}}$) are roughly equal to each other, but that of the hydrophilic phosphate ester of TBP ($\rho_{\text{hydrophilic}}$) is larger than those of both hydrocarbon chains; and (ii) with neutrons, the difference in scattering length density between the hydrophobic and hydrophilic parts of TBP (ρ_{butyl} and $\rho_{\text{hydrophilic}}$) is negligible as compared with the scattering length density of octane- d_{18} ($\rho_{\text{octane-}d_{18}}$). Note that X-rays and neutrons, respectively, enable the small-angle scattering to be effectively observed from the polar phosphate ester in the TBP assembly and from its overall structure, as shown in Figure 1. In fact, the q dependence of the obtained

scattering profiles differs greatly between neutrons and X-rays, thus elucidating the structural and characteristic features of TBP assemblies.

3-2. Coherent and Incoherent Scattering Components in SWANS Profiles. In the SWANS experiment, the scattered neutrons from the sample consist of two scattering components: $I_{\text{coh}}(q)$, which exhibits q dependence due to intra- and intermolecular interferences of neutrons from the samples, and I_{inc} , which maintains a constant value with q primarily governed by the elemental composition of the sample. To investigate the microscopic structure of TBP assemblies by SWANS in this study, decomposition of $I_{\text{coh+inc}}(q)$ into $I_{\text{coh}}(q)$ and I_{inc} is crucial because the scattering intensity level of I_{inc} is comparable with that of $I_{\text{coh}}(q)$; thus, I_{inc} acts as noise for $I_{\text{coh}}(q)$. At $q > 1.0 \text{ nm}^{-1}$, $I_{\text{coh}}(q)$ drastically changes with q , whereas I_{inc} keeps constant intensity with changing q , indicating that the q dependence of $I_{\text{coh}}(q)$ is strongly correlated with the evaluation of I_{inc} .

In general, estimating the scattering component I_{inc} is difficult through calculations based on the table of cross sections of elements because of multiple scattering and inelastic scattering.⁴⁶ Furthermore, in a strict sense, I_{inc} slightly and gradually starts to decrease in the higher- q region around $q = 6.0 \text{ nm}^{-1}$ or higher. Because the scattering intensities of $I_{\text{coh}}(q)$ and I_{inc} at such high q -region are affected by the vibrations of atoms (the well-known Debye–Waller factor),⁴⁷ the observed scattering intensities are reduced by a factor of $\exp(-Aq^2)$, where A is a constant. However, here we assume that the q dependence of I_{inc} can be neglected for simplicity as a first step of the analysis. For the appropriate evaluation of I_{inc} , we used a reference sample (octane- h_{18}) as explained in Section 2-3. Note that this experimental protocol worked well in our previously reported SANS experiment.^{48–50} In addition to our evaluation method described above, I_{inc} can also be evaluated by the calculation method of Shibayama et al., taking account of multiple scattering and cell thickness.⁵¹ The values of I_{inc} experimentally estimated in this study are close to those of the calculations for an incident neutron wavelength $\lambda = 0.7 \text{ nm}$. For example, at $\phi_{\text{TBP}} = 0.5$, $I_{\text{inc}} = 0.37 \text{ cm}^{-1}$ (present experiment) and 0.32 cm^{-1} (calculation in ref 51), which is an error of less than 15%. Accordingly, we believe that our protocol for evaluating I_{inc} is reasonable and proper in this study. For comparison, the experimentally observed net intensity $I_{\text{coh+inc}}(q)$ (colored solid lines) and the estimated $I_{\text{coh}}(q) [= I_{\text{coh+inc}}(q) - I_{\text{inc}}]$ (colored symbols) are shown in Figure 2. Note that the large contribution of I_{inc} can be recognized in a wide q region, where the contribution of I_{inc} increases in proportion to ϕ_{TBP} . On the basis of these considerations, we would like to stress that, in this study, the q dependence and intensity in SWANS profiles are never discussed without appropriate evaluation of I_{inc} . $I_{\text{coh}}(q)$ thus estimated in this manner will be discussed in the following sections.

3-3. Dependence on TBP Concentration of SWAXS and SWANS Profiles: Microscopic Observations. Figures 3a and 3b show SWAXS and SWANS profiles, respectively, obtained for TBP/octane mixtures with various ϕ_{TBP} values at 25°C . Note that the X-ray and neutron scattering profiles obtained from SWAXS and SWANS exhibit markedly different q dependence, owing to the different scattering contrasts obtained with these different probes, as explained in Section 3-1. In both SWAXS and SWANS profiles (Figure 3), the q dependence can be distinctly divided into two characteristic q -

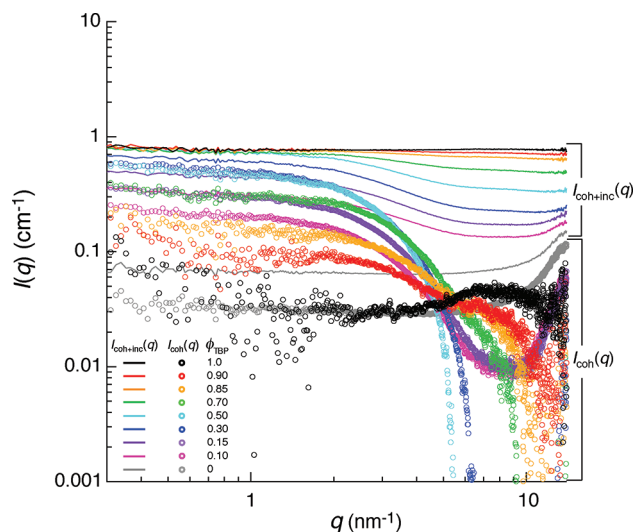


Figure 2. Comparison of the net observed SWANS profiles, $I_{\text{coh+inc}}(q)$ (colored solid lines), and coherent components for SWANS profiles, $I_{\text{coh}}(q)$ (colored open circles), obtained for TBP/octane- d_{18} mixtures as functions of ϕ_{TBP} . Error bars are omitted to show the q dependence clearly.

regions: the low- q region ($q < 6.0 \text{ nm}^{-1}$; q -region I) and the high- q region ($q > 5.0 \text{ nm}^{-1}$; q -region II), as illustrated in Figure 3.

In the low- q region, the forward scattering intensity $I(q)$ in the limit of $q \rightarrow 0$, $I(q = 0)$, depends on ϕ_{TBP} and attains a maximum at $\phi_{\text{TBP}} = 0.3$ in both SWAXS and SWANS profiles, as will be discussed in detail in Section 3-5. The absolute scattering intensities of the SWAXS profiles at $q = 0$ are smaller than those of the SWANS profiles, where the differences of the intensities mainly originate from the difference between ΔB_X^2 and ΔB_N^2 . The scattering intensity level at lower q decreases at $3.0 \text{ nm}^{-1} < q < 6.0 \text{ nm}^{-1}$ according to power law scattering, $I(q) \sim q^{-\alpha}$, where the exponent α characterizes the q dependence. The exponent α gives important and useful information about the characteristic features of the TBP assembly, including the shape, interfacial structure, and spatial distribution. These SWANS profiles at $q < 6.0 \text{ nm}^{-1}$ are quantitatively analyzed; details follow in Section 3-6.

In the high- q region, the scattering maxima I_X and I_N arise from the intermolecular dipole–dipole interactions involving the P=O groups of the phosphate esters^{1,10–12,18–20} of two TBP molecules. The scattering maxima II_X , II_N , and III_X originate from intramolecular interactions between TBP and octane. These maxima are marked with arrows in Figures 3a and 3b. At $\phi_{\text{TBP}} > 0.3$, the peak I_X around $q = 6.3 \text{ nm}^{-1}$ begins to appear (Figure 3a). Thereafter, the maximum intensity markedly increases with ϕ_{TBP} , whereas the q value at the maximum intensity (q_{IX}) slightly increases from ~ 0.63 to $\sim 0.68 \text{ nm}^{-1}$ (inset, Figure 3a). Note that this marginal shift of q_{IX} may be influenced by the change of the small-angle scattering intensity. The broad peak I_N observed in the high- q region (Figure 3b) has the same origin as peak I_X , which will be discussed in Section 3-4. In contrast, peaks II_X , II_N , and III_X are clearly independent of ϕ_{TBP} . In the SWANS profiles, only peak II_N was observed in the high- q region because the neutron scattering spectrometer used in this study is not capable of covering higher q values, such as $q > 15 \text{ nm}^{-1}$. In Figure 3b, at $q > 6.0 \text{ (nm}^{-1})$, the scattering intensity errors in the SWANS

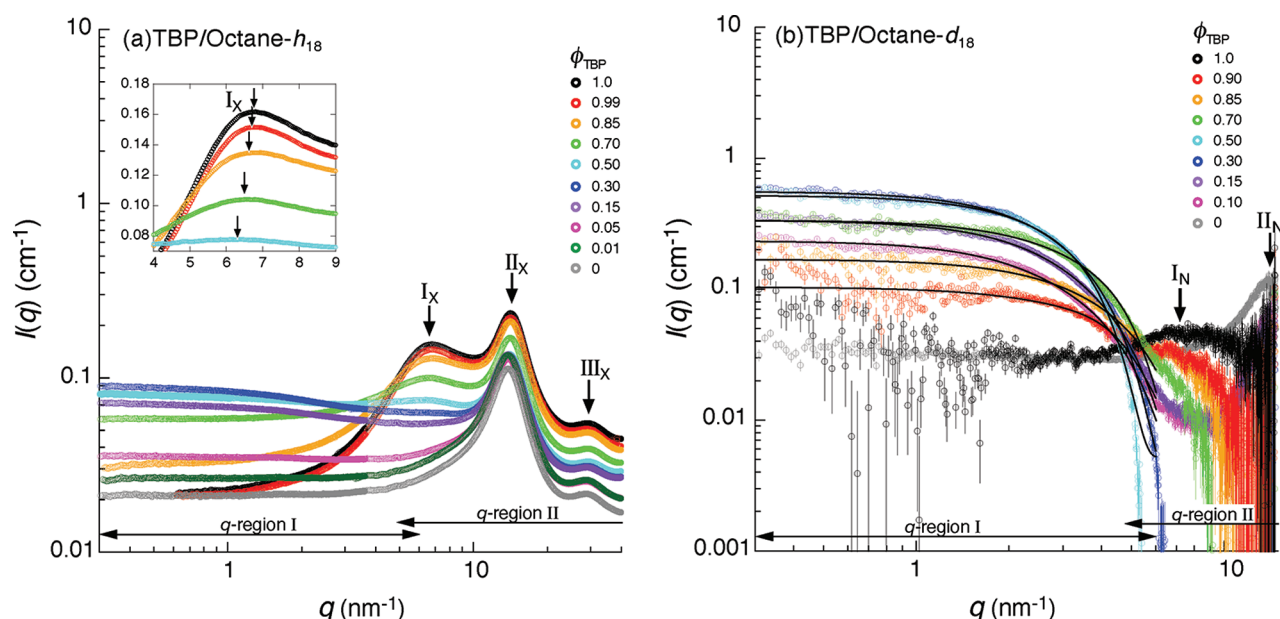


Figure 3. (a) SWAXS profiles of TBP/octane- h_{18} mixtures and (b) SWANS profiles of TBP/octane- d_{18} mixtures as functions of ϕ_{TBP} . Solid lines are the best-fit theoretical profiles obtained by using eq 3 together with the characteristic parameters listed in Table 1. Inset in (a) shows an expansion of the region between $4.0 \text{ nm}^{-1} < q < 9.0 \text{ nm}^{-1}$, illustrating the peak shift of I_X toward higher q with increasing ϕ_{TBP} . Errors in scattering intensities in the SWAXS profiles are within $\pm 0.3\%$ accuracy; for clarity, error bars are omitted.

Table 1. Summary of Characteristic Parameters Determined by the Model Analysis of the SWANS for TBP/Octane- d_{18} Mixtures

ϕ_{TBP}	R_s (nm)	R_l (nm)	R_{HS} (nm)	N_{agg}
0.1	0.5 ± 0.1	1.2 ± 0.1	0.6 ± 0.1	2.4 ± 0.8
0.15	0.5 ± 0.1	1.3 ± 0.2	0.6 ± 0.1	2.6 ± 1.0
0.3	0.5 ± 0.1	1.4 ± 0.2	0.6 ± 0.1	2.7 ± 1.0
0.5	0.6 ± 0.1	1.5 ± 0.2	0.7 ± 0.1	-
0.7	0.6 ± 0.1	1.3 ± 0.1	0.6 ± 0.1	-
0.85	0.5 ± 0.1	1.1 ± 0.2	0.6 ± 0.1	-
0.9	0.5 ± 0.1	1.0 ± 0.3	0.6 ± 0.1	-

profiles become large, and thus, a quantitative analysis could not be employed.

3-4. Evidence for TBP–TBP Association. The average distance, d_{IX} , was plotted as a function of ϕ_{TBP} on double-logarithmic scales to investigate the origin of scattering peaks I_X and I_N , where d_{IX} is defined as $d_{\text{IX}} = 2\pi/q_{\text{IX}}$ for $d_{\text{IX}} \leq 1.0 \text{ nm}$. Note that the scattering peak I_X is more suitable than I_N for quantitatively evaluating the origin of the peak because the statistical precision of I_N is worse than that of I_X (see Figure 3). Two hypotheses are considered for the origin of peak I_X : (1) the scattering among TBP molecules forming TBP assemblies, and thus, d_{IX} stands for an average distance between two TBP molecules; and (2) interparticle interference among TBP assemblies. If I_X originated from hypothesis (2), then d_{IX} should change with ϕ_{TBP} according to the following eq 1.⁵²

$$d_{\text{IX}} \sim \phi_{\text{TBP}}^{-1/3} \quad (1)$$

This relationship is indicated by a dashed straight line with slope $-1/3$ in Figure 4. However, the power law behavior of d_{IX} versus ϕ_{TBP} does not obey eq 1; instead, d_{IX} exhibits a more gradual decrease with ϕ_{TBP} as indicated by the solid line in Figure 4. This result implies that the scattering peaks I_X and I_N originate from hypothesis (1). As described above, the fact that

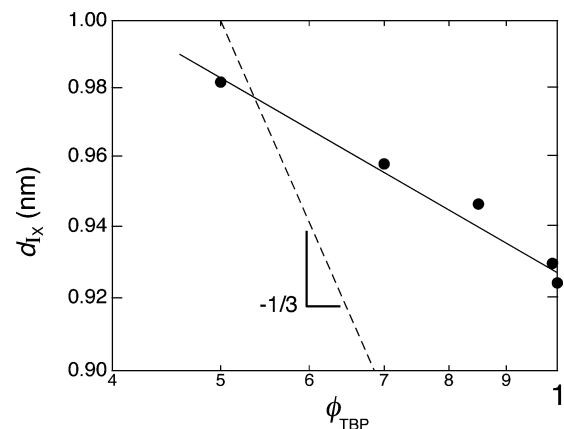


Figure 4. Average distance between TBP molecules, d_{IX} , plotted as a function of ϕ_{TBP} on double-logarithmic scales. The solid line shows the best fit to the experimental data, and the dashed line shows the prediction from eq 1.

the scattering maximum I_X is more intense than I_N also supports hypothesis (1). If hypothesis (2) were to correctly explain the origin of peaks I_X and I_N , then peak I_N should be more intense than peak I_X . This is contrary to the results obtained. Hypothesis (2) is expected to be most apparent in the SWAXS and SWANS profiles at $q < 5.0 \text{ nm}^{-1}$. On the basis of these direct observations and arguments, we conclude that TBP is not dispersed homogeneously in octane in the absence of water and heavy metal ions. Thus, TBP forms a supramolecular assembly, consistent with the extensive body of previous literature^{1,10–12,18–20} demonstrating the formation of TBP dimers.

3-5. Analysis of SWAXS and SWANS Profiles of TBP/Octane Mixtures. To investigate the ϕ_{TBP} dependence on the SWAXS and SWANS profiles, we first quantitatively characterized the dependence on ϕ_{TBP} of the scattering intensity of peak I_X (I_{IX}) and its position (q_{IX}) (see Figure 5a), when peak I_X

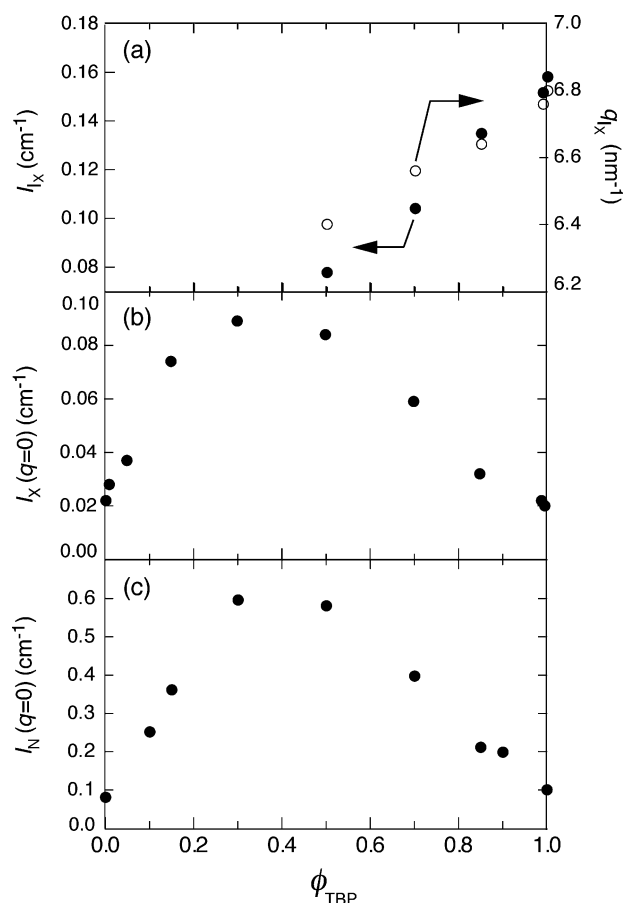


Figure 5. Four characteristic scattering parameters obtained for TBP/octane mixtures plotted versus ϕ_{TBP} : (a) I_x and q_{1x} , (b) $I_x(q=0)$, and (c) $I_N(q=0)$.

could be recognized. We also quantitatively characterized the forward scattering intensities observed by SWAXS [$I_x(q=0)$] and SWANS [$I_N(q=0)$], respectively (see Figures 5b and 5c). $I(q=0)$ depends on the osmotic compressibility of the system;^{5,53} here, $I(q=0)$ was assumed to equal the scattering intensity at the smallest q ($\sim 0.3 \text{ nm}^{-1}$) accessible in our X-ray and neutron scattering experiments (see Figure 3). Figure 5 shows these four characteristic scattering parameters as a function of ϕ_{TBP} . Peak I_x can be clearly recognized at $\phi_{\text{TBP}} > 0.5$, and I_x linearly increases with ϕ_{TBP} , indicating that the number of TBP assemblies increases with ϕ_{TBP} . At $\phi_{\text{TBP}} < 0.5$, we may reasonably presume that TBP assemblies form, even though there is no scattering maximum in the high- q region (q -region II), because in the low- q region (q -region I), the small-angle neutron scattering from the overall structure of the TBP assembly can be clearly observed at $\phi_{\text{TBP}} = 0.1$ (pink open circles) and 0.15 (purple open circles), as shown in Figure 3b. Therefore, at $\phi_{\text{TBP}} < 0.5$ TBP assemblies are also formed in octane via TBP–TBP interactions.

$I_x(q=0)$ and $I_N(q=0)$ have similar dependencies on ϕ_{TBP} , implying that both SWAXS and SWANS profiles obtained in the low- q region (q -region I) reflect the scattering contrast between a TBP assembly and octane (see Figure 1). Note that with X-rays the difference between ρ_{butyl} and $\rho_{\text{octane-h18}}$ is quite small but, nonetheless, nonzero. Thus, the small-angle scattering due to the TBP assemblies should be detected in both SWAXS and SWANS in the low- q region (q -region I).

In the context of the fluctuations theory of scattering,⁵³ $I(q=0)$ is generally given by

$$I(q=0) \sim \Delta B^2 C / \left(\frac{\partial \Pi}{\partial C} \right) \quad (2)$$

where Π is the osmotic pressure; ΔB is the scattering contrast difference between TBP and octane; and C is the concentration of TBP. At $\phi_{\text{TBP}} < 0.3$, both $I_x(q=0)$ and $I_N(q=0)$ increase with ϕ_{TBP} because of the increase in C . Conversely, at $\phi_{\text{TBP}} > 0.3$, both $I_x(q=0)$ and $I_N(q=0)$ decrease with ϕ_{TBP} . This is simply because the osmotic compressibility, $(\partial \Pi / \partial C)$, on the right-hand side of eq 2 increases with ϕ_{TBP} at $\phi_{\text{TBP}} > 0.3$, resulting in the decrease of $I(q=0)$. In such a concentrated solution, TBP assemblies tend to be dispersed homogeneously due to the strong contribution of the excluded volume effect,⁵ which acts on the TBP assemblies. As a result, the concentration fluctuations in the system are expected to be suppressed effectively.

Note that the SWAXS and SWANS obtained in this study cannot be explained by Baxter's model,^{21–23} which was formulated for extraction systems of TBP–diluent/ H_2O –acid–heavy metal ions by Chiarizia et al.^{26–39} The small-angle scattering from the reverse micelles formed by TBP in the organic phase increases at $q < 1.0 \text{ nm}^{-1}$ as the concentration of TBP, acid, water, and/or heavy metal ion increases. Using Baxter's model, they attributed the increase of scattering intensity in the low- q region to the effect of an attractive interaction between reverse micelles. In contrast to those previous results,^{26–39} in the present study, the small-angle scattering intensity in the low- q region (q -region I) decreases as the TBP concentration increases at $\phi_{\text{TBP}} > 0.3$, as shown in Figures 5b and 5c. These findings indicate that attractive interactions between TBP assemblies do not occur in dry octane as they do in wet octane. Additional evidence for this noninteracting behavior was obtained by performing a quantitative model analysis of the neutron scattering profiles, vide infra.

3-6. Quantitative Analyses of TBP Assemblies. We carried out a numerical analysis of the SWANS profiles in the low q region ($q < 6.0 \text{ nm}^{-1}$) to characterize the structure of the TBP assembly. Note that the scattering contrast of X-rays between TBP and octane, $\Delta B_X^2 [= 4.84 \times 10^{20} (\text{cm}^{-4})]$, is about 10% of that for neutrons, $\Delta B_N^2 [= 39.2 \times 10^{20} (\text{cm}^{-4})]$. In fact, the small-angle X-ray scattering intensity is relatively poor as compared with the neutron scattering, and furthermore, the power law scattering component observed in the low- q region (Porod region) and the wide-angle scattering component observed in the high- q region partially overlap in the SWAXS profiles (see Figure 3a). For this reason, SWANS profiles are more suitable than SWAXS profiles for quantitatively evaluating the shape and size of the TBP assembly, provided that the scattering contrast between neutrons and X-rays is consistent with the schematic diagram in Figure 1.

The scattering function of the TBP assembly, $I_{\text{assembly}}(q)$, is given by the product of the form factor of the assembly, $P(q)$, and its structure factor, $S(q)$

$$I_{\text{assembly}}(q) = n \Delta B_N^2 V^2 P(q) S(q) \quad (3)$$

where n is the number of TBP assemblies per unit volume in solution and V is the volume of a single assembly. At $\phi_{\text{TBP}} \leq 0.5$, n can be defined as $n = \phi_{\text{TBP}} / V$, whereas at $\phi_{\text{TBP}} \geq 0.5$, n

can be defined as $n = (1 - \phi_{\text{TBP}})/V$, where $1 - \phi_{\text{TBP}}$ is equal to the volume fraction of octane- d_{18} . Note that at $\phi_{\text{TBP}} \geq 0.5$ the TBP/octane mixtures are prone to undergo phase inversion, indicating that the small-angle scattering could be shifted for an observation object at $\phi_{\text{TBP}} = 0.5$ from the scattering of the TBP assemblies ($\phi_{\text{TBP}} \leq 0.5$) to the scattering of the microdomain structures of octane- d_{18} ($\phi_{\text{TBP}} \geq 0.5$). For $P(q)$, we employed a theoretical scattering function for the rotational ellipsoidal model. The shape of the TBP assembly is highly likely to be spherical (or ellipsoidal) due to the conformational entropy of the butyl groups of TBP. Here, $P(q)$ for an ellipsoidal particle is given by

$$P(q) = 9 \int_0^1 \left[\frac{J_1(qR_e)}{qR_e} \right]^2 dx \quad (4)$$

where $J_1(x)$ is the first-order Bessel function of x . R_e is defined as

$$R_e = R_s [1 + x^2(u^2 - 1)]^{1/2} \quad (5)$$

where R_s and u are the minor axis and the axial ratio ($u \geq 1$) of the ellipsoid, respectively. Note that in the case of a sphere u is equal to 1. As for $S(q)$, originating from the interaction among TBP assemblies or the microdomains of octane, we employed the hard sphere model given by the Percus–Yevick formalism, $S_{\text{HS}}(q)$.^{54–56} In this model, we replace the TBP assembly or the microdomain of octane with an equivalent hard sphere of radius R_{HS} , which has an excluded volume given by the sphere of radius R_{HS} and the volume fraction $\eta (= 4\pi n R_{\text{HS}}^3/3)$.⁵⁷

$$S_{\text{HS}}(q) = [1 + 24\eta G(y)/y]^{-1} \quad (6)$$

where $y = 2qR_{\text{HS}}$, and $G(y)$ is given by

$$\begin{aligned} G(y) = & (\alpha/y^2)[\sin(y) - y \cos(y)] + (\beta/y^3)[2y \\ & \sin(y) + (2 - y^2)\cos(y) - 2] \\ & + (\gamma/y^5)[-y^4 \cos(y) \\ & + 4\{(3y^2 - 6)\cos(y) + (y^3 - 6y)\sin(y) \\ & + 6\}] \end{aligned} \quad (7)$$

The quantities α , β , and γ are

$$\alpha = (1 + 2\eta)^2/(1 - \eta)^4 \quad (8)$$

$$\beta = -6\eta[(1 + (\eta/2))^2/(1 - \eta)^4] \quad (9)$$

$$\gamma = \alpha\eta/2 \quad (10)$$

The structure factor, $S(q)$, is known to be effected by the orientation of anisotropic scattering amplitudes.⁵⁸ In this case, $S(q)$ should be modified as follows

$$S(q) = 1 + \{[A(q)]^2/[\langle A(q) \rangle]^2\} [S_{\text{HS}}(q) - 1] \quad (11)$$

where $A(q)$ is the form factor amplitude of the radial scattering length density distribution. Here, three parameters— R_s , R_l , and R_{HS} —were refined to give the best fit to the data and reproduce the experimental SWANS profiles. R_l is the major axis of an ellipsoid. In this analysis, we neglected the polydispersity of R_s and R_l for simplicity. The solid lines in Figure 3b show the best-fit theoretical scattering curves and the experimental profiles (colored open circles) using eq 3. R_s , R_l , and R_{HS} , obtained for all TBP/octane- d_{18} mixtures in the concentration range of 0.1

$\leq \phi_{\text{TBP}} \leq 0.9$, are summarized in Table 1. At $\phi_{\text{TBP}} = 0$ and 1, the SWANS profiles were not fitted with eq 3 because of $\Delta B_N^2 = 0$ in a theoretical sense. This analysis indicates that the shape of TBP assemblies should be ellipsoidal and that the shape is asymmetric (i.e., not spherical). At $\phi_{\text{TBP}} \leq 0.5$, the range of u is between 2.4 and 2.8, whereas at $\phi_{\text{TBP}} > 0.5$, this range is 2.0 and 2.2. This lower range of u values is because at $\phi_{\text{TBP}} \geq 0.5$ small-angle scattering no longer provides information about the TBP assemblies and the microdomains of octane as a result of phase inversion. The values of estimated R_{HS} fall within the range between R_s and R_l , indicating that the quantitative results are internally consistent.

The aggregation number of the TBP assembly, N_{agg} , can be estimated from the obtained fitting parameters, R_s and R_l . Namely, N_{agg} is given by

$$N_{\text{agg}} = \left(\frac{4\pi}{3} R_s^2 R_l \right) \frac{d_{\text{TBP}} N_A}{M_{\text{TBP}}} \quad (12)$$

where d_{TBP} ($= 0.979$) and M_{TBP} are the density and molecular weight of TBP, respectively. N_A is Avogadro's number. Note that at $\phi_{\text{TBP}} < 0.5$ the small-angle scattering reflects the structure of the TBP assemblies as described above. Therefore, the calculation of N_{agg} is justifiable in the concentration range of $0.1 \leq \phi_{\text{TBP}} \leq 0.3$, where the values are shown in Table 1. In many previous studies,^{1,10–12,18–20} it has been reported that TBP forms a dimer in nonpolar solvents, such as cyclohexane, hexane, and dodecane. Our evaluations of N_{agg} , which show about two molecules (see Table 1, taking errors into consideration), are consistent with the historical literature on TBP dimerization. We would like to stress that the microscopic structure of TBP assemblies beyond the aggregation number—in terms of morphological details—is provided here in an original manner by use of the combined small-angle scattering techniques.

Within the framework of our quantitative analysis, $S_{\text{HS}}(q)$ could be well reproduced by the experimentally obtained scattering profiles. This result indicates that the interaction between TBP assemblies is neither attractive nor repulsive. If either attractive or repulsive interactions work between TBP assemblies, then the small-angle scattering profiles obtained would not be reproduced by $S_{\text{HS}}(q)$. Accordingly, we conclude that the attractive interaction between TBP assemblies does not occur in anhydrous octane.

3-7. Viscosity of TBP/Octane Mixtures. A crucial parameter for examining the association among TBP molecules is the viscosity of the solutions. Figure 6 shows the specific viscosity, η_{sp} , of the TBP/octane mixtures plotted versus ϕ_{TBP} . At $\phi_{\text{TBP}} < 0.3$, η_{sp} increased in proportion to ϕ_{TBP} as described by the solid line in Figure 6, whereas η_{sp} started to deviate from this linear relation and sharply increased at $0.3 < \phi_{\text{TBP}} < 0.4$. The number of TBP assemblies in the system should increase with ϕ_{TBP} ; thus, the average distance between TBP assemblies becomes relatively short at higher ϕ_{TBP} , where closer approaches are more probable than that at lower ϕ_{TBP} . The dense packing of the TBP assemblies may bring about widespread interactions among TBP molecules due to dipole–dipole interactions involving the $\text{P}=\text{O}$ groups,^{1,10–12,18–20} likely contributing to the sharp increase of η_{sp} , especially at $\phi_{\text{TBP}} > 0.3$.

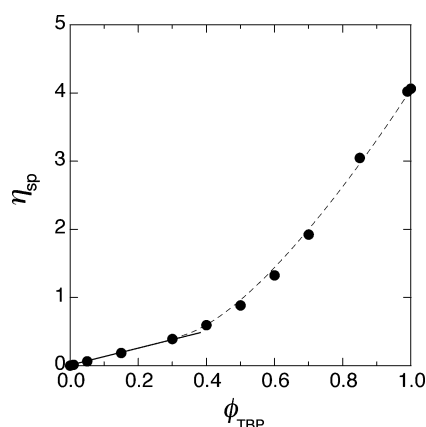


Figure 6. Specific viscosity, η_{sp} , of TBP/octane mixtures, plotted as a function of ϕ_{TBP} . The solid and dashed lines are visual guides.

4. CONCLUSIONS

We combined SWAXS, SWANS, and viscosity measurements to investigate the microscopic structure and fluidity of TBP/octane mixtures. In particular, we would like to stress that both X-ray and neutron beams are quite powerful probes for investigating the microscopic structure of TBP/octane mixtures. X-rays and neutrons enable us to focus on the inner core of the TBP assembly and the overall structure of the TBP assembly, respectively. SWAXS and SWANS with appropriate estimations of incoherent neutron scattering intensities revealed the following: (i) TBP molecules associate with each other in octane, where the distance between two TBP molecules is evaluated as 0.9–1.0 nm; and (ii) the SWANS profiles obtained for TBP/octane- d_{18} mixtures in the low- q region (q -region I) can be reproduced by a theoretical scattering model that incorporates the form factor of the rotational ellipsoid model and the structure factor of the hard sphere model. This result indicates that the shape of the TBP assembly in octane should be ellipsoid and that there is no attractive interaction between TBP assemblies in dry octane, contrary to the results obtained for TBP reverse micelles incorporating extracted water, nitric acid, and heavy metal ions in their cores. Result (i), which was directly found by SWAXS in the high- q region (q -region II), is consistent with previous reports by Osseo-Asare.⁹ These structural and characteristic features of TBP/octane mixtures revealed by SWAXS and SWANS should be useful for analyzing the structure of TBP reverse micelles incorporating extracted heavy metal ions, which will be a topic of future investigation.

AUTHOR INFORMATION

Corresponding Author

*E-mail: motokawa.ryuhei@jaea.go.jp. Tel. & Fax: +81-29-284-3747.

ACKNOWLEDGMENTS

The authors thank Dr. Hitoshi Endo for helpful discussions of X-ray and neutron scattering data. The neutron scattering experiments at SNS, Oak Ridge National Laboratory, were performed with the approval of the Scientific User Facilities Division, Office of Basic Energy Sciences, U.S. Department of Energy. The authors thank Dr. William T. Heller for generous technical support with the neutron scattering experiments at SNS. The synchrotron radiation experiments at SPring-8 were

performed with the approval of the Japan Synchrotron Radiation Research Institute (JASRI; Proposal No. 2011B1148-NL-np). This work was supported in part by the Ministry of Education, Science, Sports and Culture, Japan (Grants-in-Aid for Young Scientists (B), 2010-2011, No. 22760683). The work at Argonne is supported by the U.S. Department of Energy, Division of Chemical Science, Bioscience and Geosciences, under contract No DE-AC02-06CH11357.

REFERENCES

- (1) Schulz, W. W.; Navratil, J. D. *Science and Technology of Tributyl Phosphate, vol I; Synthesis, Properties, Reactions and Analysis*; CRC Press: Boca Raton, FL, 1984.
- (2) Naylor, A.; Wilson, P. D. In *Handbook of Solvent Extraction*; Lo, T. C., Baird, M. H. I., Hanson, C., Eds.; Wiley: New York, 1983; pp 783–798.
- (3) Rao, P. R. V.; Kolarik, Z. *Solvent Extr. Ion Exch.* **1996**, *14*, 955–993.
- (4) Glatter, O.; Kratky, O. *Small Angle X-ray Scattering*; Academic Press: London, 1982.
- (5) Higgins, J. S.; Benoît, H. C. *Polymers and Neutron Scattering*; Oxford University Press: Oxford, 1994.
- (6) Roe, R.-J. *Methods of X-ray and Neutron Scattering in Polymer Science*; Oxford University Press: New York, 2000.
- (7) Lindner, P.; Zemb, Th. *Neutrons, X-rays and Light: Scattering Methods Applied to Soft Condensed Matter*; Elsevier: Amsterdam, 2002.
- (8) Zemb, Th.; Diat, O. *J. Phys.: Conf. Ser.* **2010**, *247*, 012002.
- (9) Osseo-Asare, K. *Adv. Colloid Interface Sci.* **1991**, *37*, 123–173.
- (10) Dyrssen, D.; Petkovic, D. *J. Inorg. Nucl. Chem.* **1965**, *27*, 1381–1393.
- (11) Petkovic, D. M. *J. Inorg. Nucl. Chem.* **1968**, *30*, 603–609.
- (12) Petkovic, D. M.; Kezele, B. A.; Rajic, D. R. *J. Phys. Chem.* **1973**, *77*, 922–924.
- (13) Poczynailo, A.; Danesi, P. R.; Scibona, G. *J. Inorg. Nucl. Chem.* **1973**, *35*, 3249–3255.
- (14) Tsimering, L.; Kertes, A. S. *J. Chem. Thermodyn.* **1974**, *6*, 411–415.
- (15) Tsimering, L.; Kertes, A. S. *Thermochim. Acta* **1975**, *12*, 206–208.
- (16) Rytting, J. H.; Goldkamp, A.; Lindenbaum, S. *J. Solut. Chem.* **1975**, *4*, 1005–1010.
- (17) Petkovic, D. M.; Maksimovic, Z. B. *J. Inorg. Nucl. Chem.* **1976**, *38*, 297–300.
- (18) Kertes, A. S.; Tsimering, L.; Grauer, F. *J. Inorg. Nucl. Chem.* **1976**, *38*, 867–869.
- (19) Klatt, L. N. *Anal. Chim. Acta* **1980**, *116*, 289–296.
- (20) Choi, K.; Tedder, D. W. *Ind. Eng. Chem. Res.* **1996**, *35*, 2048–2059.
- (21) Baxter, R. J. *J. Chem. Phys.* **1968**, *49*, 2770–2774.
- (22) Menon, S. V. G.; Kelkar, V. K.; Manohar, C. *Phys. Rev. A* **1991**, *43*, 1130–1133.
- (23) Menon, S. V. G.; Manohar, C.; Srinivas Rao, K. *J. Chem. Phys.* **1991**, *95*, 9186–9190.
- (24) Liu, Y. C.; Chen, S. H.; Huang, J. S. *Phys. Rev. E* **1996**, *54*, 1698–1708.
- (25) Erlinger, C.; Gazeau, D.; Zemb, Th.; Madic, C.; Lefrançois, L.; Hebrant, M.; Tondre, C. *Solvent Extr. Ion Exch.* **1998**, *16*, 707–738.
- (26) Jensen, M. P.; Chiarizia, R.; Ferraro, J. R.; Borkowski, M.; Nash, K. L.; Thiyagarajan, P.; Littrell, K. C. In *Proceeding of the International Solvent Extraction Conference (ISEC)*, 2002.
- (27) Chiarizia, R.; Nash, K. L.; Jensen, M. P.; Thiyagarajan, P.; Littrell, K. C. *Langmuir* **2003**, *19*, 9592–9599.
- (28) Chiarizia, R.; Jensen, M. P.; Borkowski, M.; Ferraro, J. R.; Thiyagarajan, P.; Littrell, K. C. *Sep. Sci. Technol.* **2003**, *38*, 3313–3331.
- (29) Chiarizia, R.; Jensen, M. P.; Borkowski, J. R.; Thiyagarajan, P.; Littrell, K. C. *Solvent Extr. Ion Exch.* **2003**, *21*, 1–27.

- (30) Chiarizia, R.; Jensen, M. P.; Rickert, P. G.; Kolaric, Z.; Borkowski, M.; Thiyagarajan, P. *Langmuir* **2004**, *20*, 10798–10808.
- (31) Chiarizia, R.; Jensen, M. P.; Borkowski, M.; Thiyagarajan, P.; Littrell, K. C. *Solvent Extr. Ion Exch.* **2004**, *22*, 325–351.
- (32) Plae, J.; Gelis, A.; Czerwinski, K.; Thiyagarajan, P.; Chiarizia, R. *Solvent Extr. Ion Exch.* **2006**, *24*, 283–298.
- (33) Chiarizia, R.; Rickert, P. G.; Stepinski, D.; Thiyagarajan, P.; Littrell, K. C. *Solvent Extr. Ion Exch.* **2006**, *24*, 125–148.
- (34) Chiarizia, R.; Stepinski, D. C.; Thiyagarajan, P. *Sep. Sci. Technol.* **2006**, *41*, 2075–2095.
- (35) Chiarizia, R.; Jensen, M. P.; Borkowski, M.; Nash, K. L. *Sep. Nucl. Fuel Cycle 21st Century* **2006**, 933, 135–150.
- (36) Chiarizia, R.; Briand, A.; Jensen, M. P.; Thiyagarajan, P. *Solvent Extr. Ion Exch.* **2008**, *26*, 333–359.
- (37) Chiarizia, C.; Stepinski, D.; Antonio, M. R. *Sep. Sci. Technol.* **2010**, *45*, 1668–1678.
- (38) Antonio, M. R.; Chiarizia, R.; Jaffrennou, F. *Sep. Sci. Technol.* **2010**, *45*, 1689–1698.
- (39) Moyer, B. A., Ed. *Ion Exchange and Solvent Extraction: A Series of Advances*; CRC Press: Boca Raton, 2010; 19.
- (40) Nave, S.; Modolo, G.; Madic, Ch.; Testard, F. *Solvent Extr. Ion Exch.* **2004**, *22*, 527–551.
- (41) Nave, S.; Mandin, C.; Martinet, L.; Berthon, L.; Testard, F.; Madic, C.; Zemb, Th. *Phys. Chem. Chem. Phys.* **2004**, *6*, 799–808.
- (42) Antonio, M. R.; Chiarizia, R.; Gannaz, B.; Berthon, L.; Zorz, N.; Hill, C.; Cote, G. *Sep. Sci. Technol.* **2008**, *43*, 2572–2605.
- (43) Inoue, K.; Oka, T.; Miura, K.; Yagi, N. *AIP. Conf. Proc.* **2004**, *705*, 336–339.
- (44) Zhang, F.; Ilavsky, J.; Long, G. G.; Quintana, J. P. G.; Allen, A. J.; Jemian, P. R. *Metall. Trans. A* **2010**, *41A*, 1151–1158.
- (45) Zhao, J. K.; Gao, C. Y.; Liu, D. J. *Appl. Crystallogr.* **2010**, *43*, 1068–1077.
- (46) Schelten, J.; Schmatz, W. J. *Appl. Crystallogr.* **1980**, *13*, 385–390.
- (47) Squires, G. L. *Introduction to the Theory of Thermal Neutron Scattering*; Cambridge University Press: Cambridge, 1978.
- (48) Koga, T.; Tanaka, F.; Motokawa, R.; Koizumi, S.; Winnik, F. M. *Macromolecules* **2008**, *41*, 9413–9422.
- (49) Motokawa, R.; Koizumi, S.; Hashimoto, T.; Annaka, M.; Nakahira, T. *Macromolecules* **2010**, *43*, 752–764.
- (50) Terashima, T.; Motokawa, R.; Koizumi, S.; Sawamoto, M.; Kamigaito, M.; Ando, T.; Hashimoto, T. *Macromolecules* **2010**, *43*, 8218–8232.
- (51) Shibayama, M.; Nagao, M.; Okabe, S.; Karino, T. *J. Phys. Soc. Jpn.* **2005**, *4*, 2728–2736.
- (52) Shibayama, M.; Hashimoto, T.; Kawai, H. *Macromolecules* **1983**, *16*, 16–28.
- (53) Debye, P. J. *Appl. Phys.* **1944**, *15*, 338–342.
- (54) Percus, J. K.; Yevick, G. J. *Phys. Rev.* **1958**, *110*, 1–13.
- (55) Kinning, D. J.; Thomas, E. L. *Macromolecules* **1984**, *17*, 1712–1718.
- (56) Shibayama, M.; Kawada, H.; Kume, T.; Matsunaga, T.; Iwai, H.; Sano, T.; Osaka, N.; Miyazaki, S.; Okabe, S.; Endo, H. *J. Chem. Phys.* **2007**, *127*, 144507–144513.
- (57) Endo, H.; Miyazaki, S.; Haraguchi, K.; Shibayama, M. *Macromolecules* **2008**, *41*, 5406–5411.
- (58) Kotlarchyk, M.; Chen, S.-H. *J. Chem. Phys.* **1983**, *79*, 2461–2469.